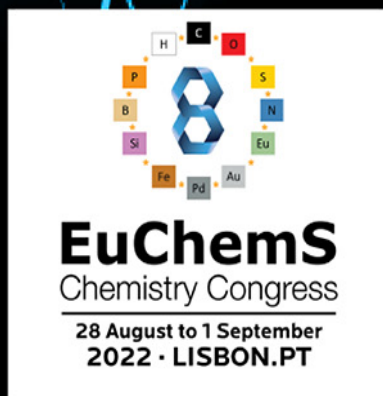


Chemistry Europe Amplifying Great Science

 **Chemistry
Europe**
European Chemical
Societies Publishing



Stop by our
booth #3

Chemistry Europe Symposium Monday, August 29, 9:15 – 12:30 Room #9

- We will celebrate the 10th anniversaries of *ChemistryOpen* and *ChemPlusChem*
- Mark the launch of *Chemistry-Methods* and *Analysis & Sensing*
- And introduce the redesign of *ChemistryViews* on a new platform

Join us for five fascinating talks by top scientists

Chem
Plus
Chem



Célia Fonseca-Guerra
Vrije Universiteit Amsterdam

Analysis &
Sensing



Francesco Ricci
Rome Tor Vergata

ChemistryViews



Javier García Martínez
Universidad de Alicante
Current President of IUPAC

Chemistry
Open



Anat Milo
Ben Gurion University

Chemistry
Methods



Ramón Martínez Mánez
Universitat Politècnica
de València

We look forward to
seeing you in Lisbon

chemistry-europe.org



Monolithic Al₂O₃ Xerogels with Hierarchical Meso-/Macropore System as Catalyst Supports for Methanation of CO₂

Ken Luca Abel,^[a] Tobias Beger,^[a] David Poppitz,^[a] Ronny T. Zimmermann,^[b] Oliver Kuschel,^[a] Kai Sundmacher,^[b, c] and Roger Gläser*^[a]

Cylindrical, cm-sized monolithic Al₂O₃ xerogels with hierarchical meso-/macropore system were prepared by sol-gel synthesis. The influence of both solvent exchange and drying on monolith stability and the resulting pore system was studied following mass and volume of the monolith as well as by porosimetry and electron microscopy. Crack-free drying of the monoliths requires a proper management of drying stress. This is achieved by adjusting the drying rate and solvent exchange procedure

applied to the intermediate lyogels. Moreover, mainly through differences in capillary pressure, changing the pore fluid allows an adjustment of the mesopore width from 7.6 nm to 10.5 nm. Neither solvent exchange nor drying affect the macropores, the width of which stays at 1.5 μm. Finally, CO₂ methanation over Ni-impregnated Al₂O₃ monoliths reveals CO₂ conversion and CH₄ selectivity comparable to an industrial Ni/Al₂O₃ benchmark catalyst.

Introduction

In response to global warming caused by the increase of greenhouse gas emissions,^[1] a shift from fossil-fuel powered power plants towards renewable energy sources is on its way.^[2] However, owing to the intermittent energy supply of renewables, surpluses and shortages of energy generation may occur. An attractive approach to compensate for this is the storage of renewable surplus energy in chemical bonds as part of the "Power-to-X" technologies. A major challenge of this approach is the coupling of chemical processes to renewable energy generation. Hence, these processes are necessarily subject to the fluctuating energy supply. Recent research efforts have focused on more flexible operation concepts of chemical

processes.^[3] In this regard, the methanation of CO₂ with renewable H₂ as an example for Power-to-Gas technology is an attractive approach, due to the potential to directly inject methane into the gas grid.^[4] Typically conducted in fixed-bed reactors, proper heat management is one of the key challenges for the exothermic CO₂ methanation reaction.^[5] Indeed, severe hotspot formation during CO₂ methanation has been proven both by simulation and experimental studies.^[6] Using conventional catalyst particles with homogenous distribution of active components, it has been shown that hotspots form during start-up of the reactor and may be sustained for some time even after cooling down as consequence of wrong-way behavior.^[7,8] More frequent reactor start-ups and shut-downs may be a relevant dynamic operation scenario in future. To address this, Zimmermann *et al.* have recently investigated the use of non-uniform catalyst particles.^[9,10] It was found that core-shell catalysts, *i.e.*, pellets consisting of a catalytically active core surrounded by an inactive shell, result in a faster start-up and shut-down of the reactor compared to uniform catalyst particles. More importantly though, wrong-way behavior is avoided, and parametric sensitivity studies reveal broad operation regimes in terms of coolant temperature, reactor pressure and inlet gas velocity. These superior properties arise from a high intrinsic activity of the core-shell catalyst at low temperatures, while mass transfer limitations at high temperatures avoid the formation of hotspots beyond critical deactivation temperatures.


While the studies of Zimmermann *et al.*^[8,9] present core-shell type catalysts as promising materials for the dynamically operated methanation of CO₂, they also emphasize the importance of control over catalyst pellets on the pellet scale. This includes not only the size and shape of the pellets, but also their pore system, as this will affect both heat and mass transport within the pellet.


[a] K. L. Abel, T. Beger, Dr. D. Poppitz, O. Kuschel, Prof. R. Gläser
Institute of Chemical Technology
Universität Leipzig
D-04103 Leipzig (Germany)
E-mail: roger.glaeser@uni-leipzig.de

[b] R. T. Zimmermann, Prof. K. Sundmacher
Chair for Process Systems Engineering
Faculty of Process & Systems Engineering
Otto von Guericke University Magdeburg
D-39106 Magdeburg (Germany)

[c] Prof. K. Sundmacher
Department Process Systems Engineering
Max Planck Institute for Dynamics of Complex Technical Systems
D-39106 Magdeburg (Germany)

 Supporting information for this article is available on the WWW under <https://doi.org/10.1002/cctc.202200288>

 This publication is part of a joint Special Collection with ChemElectroChem on "Catalysts and Reactors under Dynamic Conditions for Energy Storage and Conversion (DynaKat)". Please check our homepage for more articles in the collection.

 © 2022 The Authors. ChemCatChem published by Wiley-VCH GmbH. This is an open access article under the terms of the Creative Commons Attribution Non-Commercial License, which permits use, distribution and reproduction in any medium, provided the original work is properly cited and is not used for commercial purposes.

For the methanation of CO₂ with hydrogen, alumina-supported Ni catalysts are most frequently used, since they exhibit a favorable balance between activity, selectivity and cost.^[5,11] Though the applied Ni/Al₂O₃ catalysts are often mesoporous,^[12] optimization of or a rational control over the pore system is typically not a focus in the analysis of the methanation catalysts.

Recently, we have studied the use of hierarchically porous Ni/Al₂O₃ xerogels prepared from sol-gel synthesis combined with polymerization-induced phase separation.^[13] This synthesis method allows the adjustment of both meso- and macropore widths and volume fractions.^[14,15] Furthermore, as reported by several authors,^[14,16,17] porous Al₂O₃ monoliths can be prepared by evaporative drying. Unfortunately, details of the drying procedure are usually not reported, despite the often-highlighted importance of this synthesis step for the mechanical stability of the resulting xerogels.^[18,19]

In fact, most of the current understanding of gel drying was developed for SiO₂ monoliths and originates from research by Sherwood in 1929^[20] and the early 1930s. Following this pioneering work, the theory of fluid transport and drying theory was extensively studied by Scherer in the late 1980s.^[21,22,23] Since then, computational progress has allowed more rigorous treatment of mass- and heat transport in porous bodies,^[24] such that drying and cracking can be more accurately predicted. The mechanistic understanding of the drying process, however, has not changed much over the past 30 years, leaving the work of Brinker and Scherer^[22] still as the most important reference point even for work reported in recent literature.^[18,25,26]

It is widely accepted that drying of porous bodies follows three stages. The first stage is the constant rate period (CRP), since the evaporation rate in this phase is approximately constant. The large majority of the mass loss and shrinkage of a gel body occurs during CRP. The reason for the shrinkage is that the pore liquid will cover the exposed surface by going into tension, known as capillary forces. For a cylindrical pore, the capillary pressure P_c can be expressed in terms of the surface tension γ , the pore radius r and the contact angle θ by the Young-Laplace equation (Eq. [1]),^[23]

$$P_c = -\frac{2\gamma\cos(\theta)}{r} \quad (1)$$

the negative sign indicating that the liquid is in tension. The capillary tension is balanced by the solid phase, which therefore compresses, resulting in shrinkage. As evaporation occurs at the exterior surface, liquid is drained from the interior by flow according to the Darcy law (Eq. [2]).^[22]

$$J = -\frac{D}{\eta}\nabla P_L \quad (2)$$

The liquid flow is expressed by the Flux J and dependent on the dynamic viscosity of the liquid η , the permeability D and the pressure gradient ∇P_L originating from the surface tension of the solvent. As long as the gel is compliant, P_c remains small, thus shrinking continues. However, with decreasing volume, the

gel network stiffens, until it is stable enough to withstand the capillary pressure. At this so-called critical point, shrinkage stops, and the transition to the second drying phase, the so-called first falling rate period, occurs. The beginning of this phase is marked by the liquid-vapor-interface entering the pores of the gel body. However, most of the pore liquid evaporates still at the exterior surface of the gel body, while Darcy flow continues through a thin film. Eventually, liquid flow from the interior of the body cannot be sustained, so removal of pore fluid is only possible by liquid evaporating inside and diffusing out of the gel body. This marks the transition to the second falling rate period.

Fracture during monolith drying is often described as a consequence of the high capillary forces acting upon the solid network.^[19] However, this is an oversimplification. Rather, cracking results from a phenomenon called drying stress.^[22,23,26] Since the exterior regions of the monolith dry faster than the interior ones, a pressure gradient, described by the Darcy law (Eq. [2]), develops inside the pore liquid. This in turn exerts a gradient of compressive forces on the solid phase. As a result, the exterior part of the gel body stretches, i.e., shrinks slower than its natural rate, while the interior part is compressed, i.e., shrinks faster than its natural rate. This generates tension in the material, which ultimately causes fracture, particularly at the exterior surface of the gel body.^[22] In this regard, it is important to point out that it is not the strength of the capillary pressure itself, which causes cracking. Instead, it is the difference in pressure exerted across the material. In fact, the impact of capillary pressure on fracture is only an indirect one, since capillary forces impact the pore width (Eq. [1]), which itself is related to the square root of the permeability D (Eq. [2]).^[23] Based on these considerations, slow drying, aging, use of pore fluids with low surface tension and larger pores are recommended to avoid fracture of gel bodies during drying.^[26]

In this article, a preparation procedure for a facile, reproducible synthesis of cm-sized Al₂O₃ xerogels with controllable, hierarchical meso-/macropore system is reported. A detailed study of the post-gelation events, in particular solvent exchange and drying, is conducted to evaluate their importance on monolith stability and the resulting pore structure. Additionally, a Ni-impregnated Al₂O₃ xerogel is investigated in the catalytic methanation of CO₂ with H₂ to study the applicability of the Al₂O₃ monoliths as a catalyst support.

Results and Discussion

Effect of solvent exchange and drying on monolith stability

For the preparation of Al₂O₃ xerogel monoliths, we follow the approach published by Herwig *et al.*^[27] and by our group,^[13] but focus on the stability of gel bodies. The synthesis was originally developed by Tokudome *et al.*,^[14] who reported that stable Al₂O₃ gel bodies can be obtained after evaporative drying at 313 K. Therefore, evaporative drying was also used in this study.

Figure 1 shows photographs of Al₂O₃ gels, to which no solvent exchange was applied after gelation and aging. While

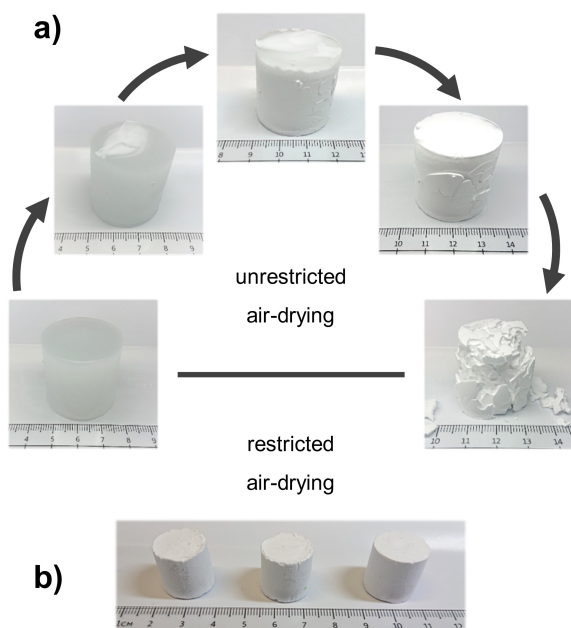


Figure 1. Photographs of Al_2O_3 gels prepared without solvent exchange after gelation and drying in ambient air; a) without restriction of drying rate; b) xerogel calcined at 973 K after drying in closed plastic container with 25 punctuations ($d=0.9$ mm) in lid.

the material in Figure 1a was dried under ambient air without any restriction on the drying rate, the dried Al_2O_3 gels in Figure 1b were obtained by drying under ambient air within closed polypropylene containers with 25 punctuations ($d=0.9$ mm) in the lid.

As evident from Figure 1, unrestricted drying results in the fracture of the gel, while the reduction of the drying rate allows the monoliths to dry essentially crack-free. This finding can be rationalized by the concept of drying stress as described in the introduction section. Clearly, the surface of the monolith in Figure 1a dries faster than the rest of the gel body, as visible by the opaque spots. Cracks then form primarily on the outside of the gel body. Eventually, further fracture occurs, such that the monolith breaks apart. As drying stress is the assumed reason for the fracture of the monolith during unrestricted air-drying (Figure 1a), a reduction of the drying rate can be considered an effective countermeasure against cracking. Indeed, drying with restricted drying rate (Figure 1b) avoids crack formation. This is a remarkable result, since the reduction of both diameter and height from initially 31 mm to 18 mm in the dried state represents a shrinkage of about 80 vol.%. However, it took 123 days to dry the monoliths to mass constancy, which identifies drying without solvent exchange as a possible, yet non-practical approach to prepare Al_2O_3 monoliths in the cm-size regime.

To reduce the necessary time for drying of the Al_2O_3 lyogels, the pore fluid was exchanged with ethanol (EtOH), acetone and *n*-pentane by two different methods after aging. These solvents were chosen because of their lower vapor pressure, surface tension and viscosity compared to H_2O (Table 1). After solvent exchange, the lyogels were dried either in ambient air with

	P_{sat} (293 K) [hPa]	γ (298 K) [mN m ⁻¹]	η (298 K) [mPa · s]
H_2O	23	71.99	0.890
EtOH	58	21.97	1.074
acetone	246	22.72	0.306
<i>n</i> -pentane	562	15.49	0.224

reduced drying rate (Figure 1b) or over a molecular sieve in a desiccator. Three replicates of each solvent/exchange-method/drying-method combination, hereafter referred to as “batch”, were prepared to increase the statistical accuracy of the results.

The relative masses and corresponding standard deviations obtained during drying of the monoliths prepared in this way are shown in Figure 2. The observed total mass loss during drying was approximately 80 wt% for all batches, indicating that a similar mass of solvent evaporated during drying. Figure 2a shows the relative gel body masses for gels drying

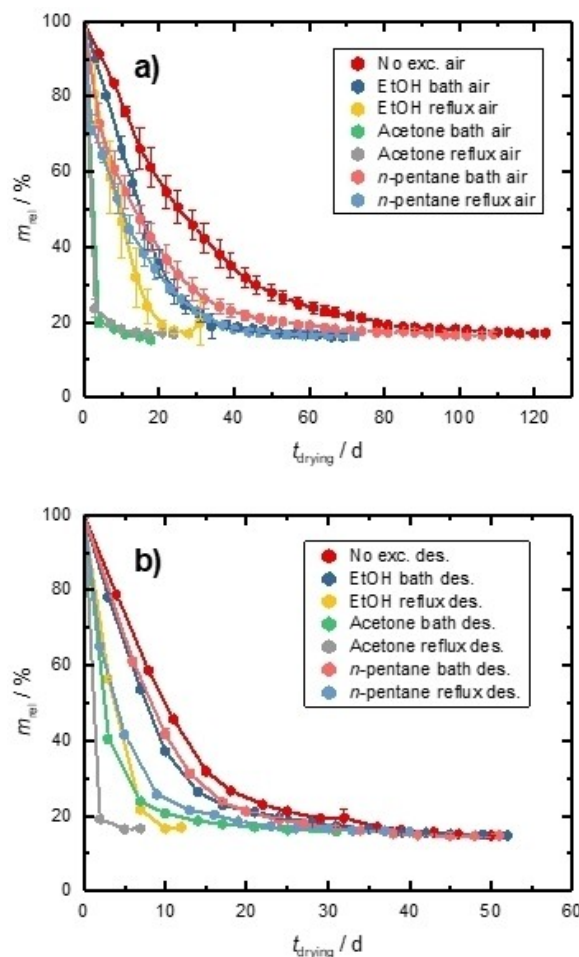


Figure 2. Average relative gel body mass of monoliths; a) drying under ambient air with restricted drying rate; b) drying in a desiccator over molecular sieves. Standard deviations of average relative masses are indicated by error bars.

under ambient air with restricted drying rate. Clearly, an increase of the drying rate is observed as a result of solvent exchange. The fastest evaporation is achieved by refluxing the gel bodies in acetone, which reduced the necessary drying time (mass constancy) from 123 to 19 days. An even faster drying is observed, if the lyogels are dried in a desiccator over a molecular sieve (Figure 2b). In fact, the drying time in absence of any solvent exchange is reduced from 123 to 50 days merely by changing from air- to desiccator drying, indicating a higher evaporation rate achieved by this method. This finding applies to all pairs of batches with identical solvent/ solvent-exchange combination. A much more important difference between the two drying methods is the observed standard deviation of the loss of relative gel body mass during drying. While for air-drying (Figure 2a) error bars can be clearly identified, especially for batches with longer drying times, they are < 2% for desiccator drying (Figure 2b), thus not visible. This finding is much more important, since it demonstrates a much higher reproducibility of the desiccator drying method compared to that of air-drying. This high reproducibility is due to the defined, approximately constant atmosphere in the desiccator with the drying agent constantly removing solvent vapor from the gas phase. Thus, air-drying is much more sensitive to local fluctuations of, for example, temperature, air pressure and moisture, which may affect monolith drying.

Another advantage of the desiccator drying route is the ability to adjust the drying rate by the choice and mass of the drying agent. As demonstrated in Figure 3a), the evaporation rate can indeed be slowed down by the lowering the drying agent mass from 4 to 1 g mmol⁻¹, resulting in the prolongation of drying time from 7 to 18 days. Yotsuyanagi *et al.*^[28] investigated the use of a desiccator to dry calcium alginate gels over silica gel. It was found that H₂O removal was faster than for drying the gels at room temperature, though it was slower compared to drying at 383 K. Unfortunately, no statement on the reproducibility of the drying method was made. Nevertheless, based on our results, desiccator drying represents as a simple, yet very reliable drying method.

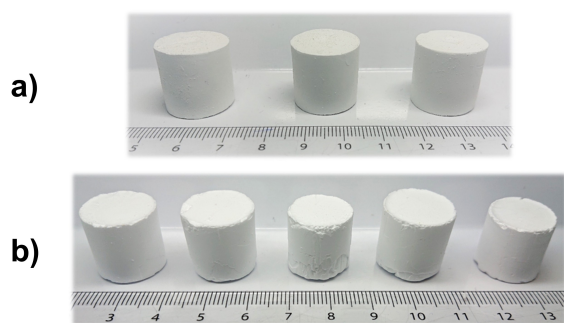


Figure 3. a) Average relative gel body masses of Al₂O₃ monoliths calcined at 973 K refluxed in acetone, dried in a desiccator over varying amounts of drying agent. Standard deviations of average relative masses are indicated by error bars; b) pore width distribution (solid lines) and cumulative specific pore volume (dashed lines) of these Al₂O₃ xerogels, determined by Hg porosimetry.

Aside from the drying method, solvent exchange has a substantial effect on the evaporation rate. For both air- and desiccator drying (Figure 2), evaporation rates are higher, if a reflux procedure is used instead of exchange in a solvent bath. This indicates that refluxing in the solvent leads to a more efficient solvent exchange, *i.e.*, a higher fraction of solvent is exchanged, compared to the solvent bath procedure. Additionally, the drying rate is influenced to a great extent by the nature of solvent applied. The lack of solvent exchange results in the slowest drying rate. With solvent exchange though, drying proceeds faster in the order *n*-pentane < EtOH < acetone. These observations can be explained by analysis of the vapor pressure during drying. Evaporative drying exerts capillary pressure P_c on the pore liquid, such that its vapor pressure P_v is reduced according to the Kelvin equation for cylindrical pores (Eq. [3]),^[22,29]

$$P_v = P_{\text{sat}} \exp\left(-\frac{P_c V_m}{RT}\right) = p_0 \exp\left(\frac{\gamma V_m}{rRT}\right) \quad (3)$$

with the molar volume of the liquid V_m and the universal gas constant R . It is evident from Equation (3) that the liquid vapor pressure depends on the saturation vapor P_{sat} of the solvent. Moreover, recalling that evaporation occurs from a concave meniscus ($r < 0$), vapor pressure is increased, if the surface tension of the liquid decreases. Saturation vapor pressures and surface tensions of the solvents applied in this article are given in Table 1.

In the absence of solvent exchange, the pores of the lyogel bodies are filled with an EtOH/H₂O mixture. The molar ratio of these solvents is initially $n_{\text{EtOH}}/n_{\text{H}_2\text{O}} = 5.4/18.1$, defined by the precursor solution, but probably shifted in favor of H₂O, as gelation and aging processes progress. The presence of H₂O inside the pores explains the relatively slow drying rate, since H₂O exhibits the lowest saturation vapor pressure and highest surface tension compared to the other solvents used in this study (Table 1). From the data in Table 1, it is clear that acetone exchange results in a higher drying rate compared to EtOH, which itself leads to faster drying than no solvent exchange.

An additional effect of solvent exchange was found by CHN elemental analysis on selected, dried Al₂O₃ gels. Without solvent exchange, the carbon mass fraction of the dried gels was 7–8 wt.%, compared to 2–4 wt.%, if EtOH exchange in a solvent bath was applied. Given that the liquid expelled from the lyogel prior to drying is insufficient to dissolve all of the used PEO, most of the remaining carbon after drying can be ascribed to this polymer. Since PEO tends to swell in H₂O and EtOH, its interaction with these solvents probably slows down solvent evaporation. Therefore, removal of the polymer by solvent exchange likely contributes to the increased drying rate. This probably also reduces the risk of fracture during calcination by pyrolysis or oxidative removal of remaining carbon.

Equation (3) does not, however, explain why *n*-pentane exchange results in a drying rate slower than EtOH exchange. Most likely, this finding is due to the poor miscibility between *n*-pentane and H₂O. It is conceivable, that the applied solvent exchange procedure removed only a significant fraction of

EtOH from the pores, such that a large fraction of H₂O remained. This reasoning is supported by the observation, that after an initially high evaporation rate, drying slows down rapidly after just a few days (Figure 2a). Besides, a petrol-type odor was noticed at the start of the drying procedure, which changed to an alcoholic odor at the second weighing and measuring event. In this regard, multiple exchanges, in particular EtOH/*n*-pentane and acetone/*n*-pentane, were studied. Figure S1 in the ESI shows the relative mass and volume loss of an example for the EtOH-*n*-pentane combination. Indeed, consecutive EtOH/*n*-pentane exchange resulted in complete drying within just 4 days, which is faster than the reflux acetone-desiccator batch (Figure 2b). However, the monolith was cracked severely and broke apart after the first day of drying. Most likely, this is a result of excessive drying stress by the high drying rate. In principle, it should be possible to dry monoliths successfully exchanged with *n*-pentane, if the drying rate is adjusted accordingly. However, this question was not investigated further.

Considering the previous statements, aging processes, *i.e.*, Ostwald ripening or syneresis^[22] or the different strength of capillary forces could have both impacted the pore width. Therefore, they may have had an impact on the drying rate following Equation (3). Indeed, solvent exchange effects have on multiple occasions been explained by aging processes.^[15,31] However, in these cases, solvent exchange was accompanied by a change of pH and/or increased temperature. Therefore, the individual contributions of aging processes and the replacement of pore fluid could not be separated. In this study, an aging step at 328 K for 24 h was included before solvent exchange. Since aging processes are believed to be irreversible in inorganic gels,^[22] we assume that most of the gel aging processes occur during the intentional 24 h-step, such that its effect during solvent exchange is low. The influence of solvent exchange on aging processes is further discussed in the next section, which also covers the impact of the solvent exchange procedure on the pore width distribution.

With the exception of samples dried from *n*-pentane, crack-free drying was achieved for all monoliths represented in Figure 2. Photographs of calcined Al₂O₃ xerogels, depicted in Figure 4, confirm the reproducible preparation of stable monoliths. Therein, Figure 4a represents the batch, which originates from refluxing in acetone followed by desiccator drying. These materials were dried within a remarkably short time period of only 5 days at room temperature.

The successful drying of the Al₂O₃ monoliths is somewhat surprising, since it is achieved despite an increased drying rate. As explained above, this increases the risk of drying stress as a consequence of an evolving pressure gradient (Eq. [2]). Two explanations for this finding are conceivable: First, we consider desiccator drying as an efficient, yet gentle drying method. The principle behind restricted air-drying is that the closed container allows the vapor pressure of the solvent to reach its saturation value. When this point is reached, the drying rate is essentially controlled by the diffusion of the vapor out of the container. While this is a gentle method, it is inefficient since the monolith is likely to dry at a rate slower than tolerable in

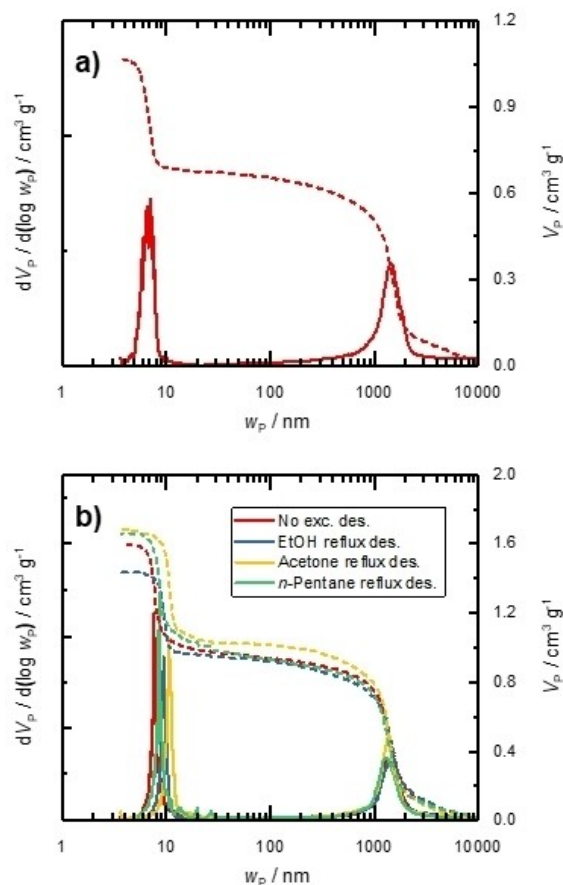


Figure 4. Photographs of Al₂O₃ xerogel monoliths calcined at 973 K after dried drying in a desiccator over molecular sieves; a) solvent exchange conducted by refluxing in acetone; b) solvent exchange carried out in EtOH bath for 7 days.

terms of monolith stability. Unrestricted drying, however, does not allow a liquid-vapor-equilibrium to set up. Instead, it even allows for fluctuations of ambient pressure, temperature, or a convective flow across the monolith surface to occur. This may result in the monolith drying too fast, such that drying stress leads to gel fracture.

Desiccator drying, however, may have represented a proper balance between the two extremes of air-drying. While the closed system of the desiccator allows an initial liquid-vapor equilibrium to form, vapor is constantly removed by the atmosphere by the drying agent. The amount of drying agent was chosen in a way, such that the mass of the evaporating solvent approximately matches the adsorption capacity of the molecular sieve. This choice may well have supported the crack-free drying, since due to the declining number of available adsorption sites for the solvent molecules, the adsorption rate likely slowed down towards the final stages of the drying process. Owing to the experimental setup, drying kinetics are coupled to the adsorption kinetics of the molecular sieve, thus a reduction of the drying rate follows inevitably. This reduction of drying rate towards the critical final phase may have protected the monolith from developing drying stress. Interest-

ingly, Saha reported avoidance of crack formation during Al_2O_3 xerogel drying by placing gel bodies inside a desiccator over CaCl_2 already in 1997.^[32] Unfortunately though, no explanation of this effect was offered. the permeability of the gel network.

A second explanation is that the increased drying rate may have been compensated by an increase of both solvent mobility and the permeability of the gel network. For example, the bulk viscosity of acetone is much lower compared to EtOH and H_2O (Table 1). Hence, the pressure gradient, which builds up according to the Darcy law (Eq. [2]), is reduced. Additionally, EtOH and acetone probably interact less strongly with the highly polar Al_2O_3 network, thus exhibiting an increased mobility in the gel network compared to H_2O . Finally, the capillary pressure acting upon EtOH and acetone is much lower than H_2O due to their lower surface tensions (Table 1). Hence, less compression of the gel network is expected, which may result in higher pore widths, and therefore increases the permeability of the gel network.^[26] This effect is studied in detail in the following section. The photographs in Figure 4 demonstrate the successful, reproducible preparation of crack-free Al_2O_3 xerogels monoliths with final diameters and heights of about 17 mm. This is equivalent to a total monolith shrinkage of 84 vol.%. About 76 vol.% of the total shrinkage occurs during drying, since the approximate diameter and height of the monoliths is 19.5 mm. This emphasizes the vital importance of controlled drying for the preparation of stable monoliths. We admit that the hierarchical nature of the pore system (Figure 5) is surely highly useful for this result because the absence of macropore volume would have required additional shrinkage and restricted liquid transport during drying. Nevertheless, following the synthesis protocols presented here, we report that crack-free Al_2O_3 xerogels monoliths in the cm-size dimensions can be prepared after drying within just one week.

Influence of solvent exchange and drying on the pore system

The pore width distribution and specific cumulative pore volume of an Al_2O_3 xerogel dried without any solvent exchange under ambient air with restricted drying rate (Figure 1b) is shown in Figure 5a. The material exhibits a bimodal pore system, resulting from polymerization-induced phase separation.^[14,33] Recently, we proved that the meso-/macropore system of Ni-containing Al_2O_3 xerogels from the synthesis approach presented here is in fact of a hierarchical nature.^[13,34]

SEM micrographs (Figure 6), revealing mesopores within the pore walls of the macroporous gel network, confirm this finding also for the xerogels of this study. As determined by Hg porosimetry, (Figure 5b), the meso- and macropore width of the calcined xerogel are 7.1 nm and 1.5 μm , respectively. About 60% of the total specific pore volume of 1.07 $\text{cm}^3 \text{g}^{-1}$ arise from macropores, the remaining 40% from mesopores. Following the effect of solvent exchange on the drying rate as discussed in the previous section, the obvious question arises, if solvent exchange likewise affected the pore system. In fact, a higher drying rate can partially be explained by an increase of the pore width according to Equation (1). Therefore, xerogels obtained

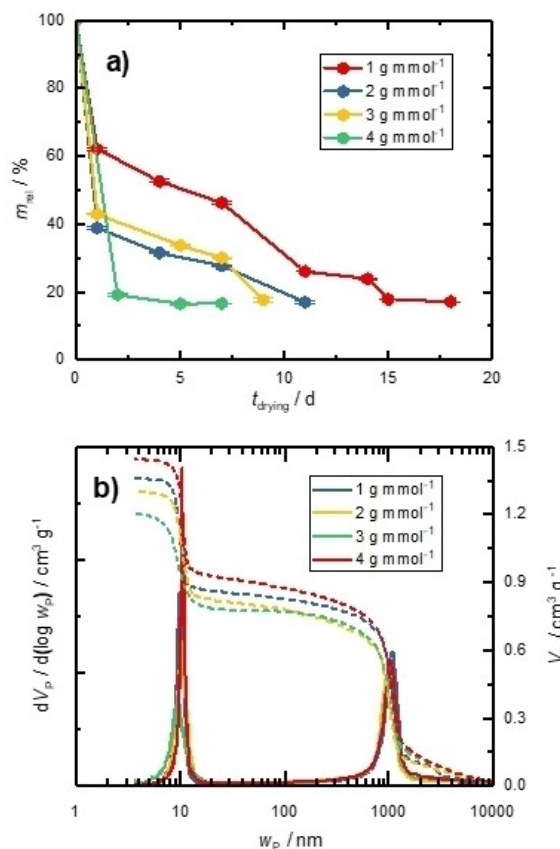


Figure 5. Pore width distribution (solid line) and specific cumulative pore volume (dashed line), determined by Hg porosimetry, of a) Al_2O_3 xerogel calcined at 973 K prepared without solvent exchange and dried under ambient air; b) Al_2O_3 xerogels calcined at 973 K, which underwent solvent exchange by refluxing and/or desiccator drying.

from reflux solvent exchange and desiccator drying (Figure 2b) were analyzed with Hg porosimetry. A representative selection of pore width distributions and specific cumulative pore volumes is presented in Figure 5a. Averages and corresponding standard deviations of meso- and macropore widths as well as specific meso- and macropore volumes are given in Table 2.

As illustrated in Figure 5a, solvent exchange did not affect the macropores of the xerogels in a significant way. Thus, both macropore width and specific macropore volume are identical

Table 2. Average ($\langle \rangle$) and standard deviation (std. dev.) of mesopore width ($w_{p,\text{meso}}$), macropore width ($w_{p,\text{macro}}$), specific mesopore volume ($V_{p,\text{meso}}$) and specific macropore volume ($V_{p,\text{macro}}$) of Al_2O_3 xerogels calcined at 973 K, which underwent solvent exchange by refluxing and/or desiccator drying. Data based on three replicates and determined by Hg porosimetry.

	no exc.	EtOH	acetone	<i>n</i> -pentane
$\langle w_{p,\text{meso}} \rangle$ [nm]	7.6	9.6	10.5	8.6
std. dev. [nm]	0.2	0.3	0.2	0.3
$\langle V_{p,\text{meso}} \rangle$ [$\text{cm}^3 \text{g}^{-1}$]	0.68	0.53	0.64	0.64
std. dev. [$\text{cm}^3 \text{g}^{-1}$]	0.06	0.03	0.05	0.08
$\langle w_{p,\text{macro}} \rangle$ [μm]	1.5	1.5	1.5	1.4
std. dev. [μm]	0.2	0.2	0.2	0.1
$\langle V_{p,\text{macro}} \rangle$ [$\text{cm}^3 \text{g}^{-1}$]	1.00	0.96	1.00	0.92
std. dev. [$\text{cm}^3 \text{g}^{-1}$]	0.05	0.03	0.03	0.06

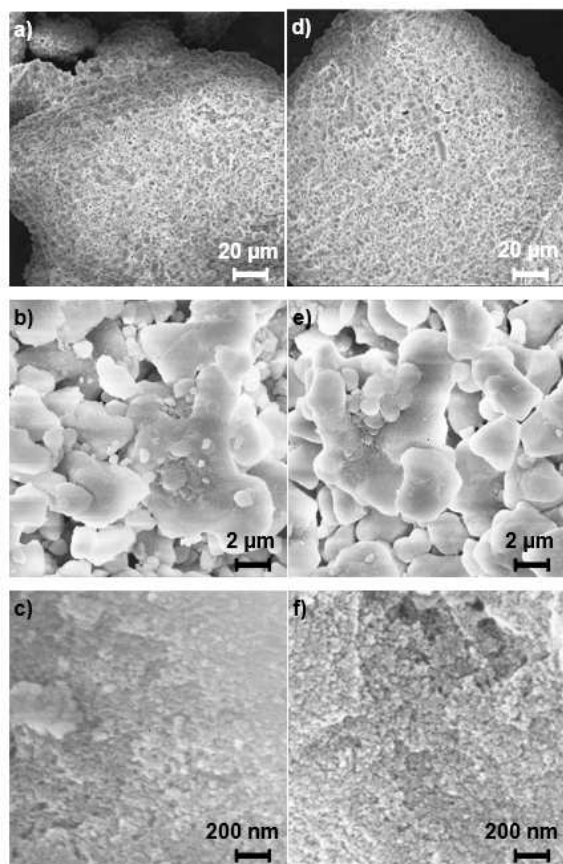


Figure 6. SEM micrographs at different magnifications; a), b) and c) Al_2O_3 support calcined at 973 K; d), e) and f) $8\text{Ni}/\text{Al}_2\text{O}_3$.

within experimental variability (Table 2). However, the mesopores of Al_2O_3 xerogels are affected by solvent exchange. Absent solvent exchange, the average mesopore width is 7.6 nm, which increases in the order n -pentane < EtOH < acetone up to 10.5 nm. This represents a significant increase (Table 2). The enlargement of the mesopores may be explained by three components, which are (1) the different strength of capillary forces, (2) temperature-induced aging processes and (3) different drying rates. In terms of the capillary forces, Equation (1) predicts a linear relationship between capillary pressure and surface tension. Lower capillary pressure means, that less compressive force is exerted on the network during drying. This ultimately allows less contraction of the pores, such that a higher pore width remains for solvents with lower surface tension. Considering the assumed low solvent exchange efficiency, this explanation is consistent with the mesopore width of the n -pentane exchanged material being only ~ 1.0 nm higher compared to no solvent exchange. However, the mesopore width of the EtOH- and acetone-exchanged gels should be similar. This is because the surface tensions of EtOH and acetone are comparable, but substantially lower than H_2O (Table 1). Although higher compared to no exchange, the average mesopore width of the acetone-exchanged samples xerogels is also 0.9 nm higher than the EtOH-exchanged

analogue (Table 2). This indicates the involvement of another factor impacting drying.

While a difference in wetting angle must be noted as a potential reason (Eq. [1]), aging processes appear to be the most likely explanation for the difference in mesopore width arising from EtOH exchange compared to acetone. This is supported by the comparison of specific mesopore volumes in Table 2. While acetone- and n -pentane exchange did not significantly alter the mesopore width compared to no solvent exchange, a decrease of specific mesopore volume is detected for the EtOH-exchanged materials. The lyogels of these were treated at 352 K, which is higher than the temperature of the aging step in mother liquor preceding solvent exchange (328 K). Therefore, refluxing in EtOH may well have led to aging processes in the form of syneresis.^[23] During syneresis, surface M-OH groups in close proximity condensate, resulting in gel network contraction and expulsion of pore liquid. Thus, different from the other solvent exchange treatments, aging processes during EtOH refluxing are not negligible, and likely responsible for a decrease of pore width and specific mesopore volume.

The third potential factor for the different mesopore widths in Figure 4b and Table 2 is the drying rate. In fact, absent solvent exchange, the faster desiccator-drying resulted in a higher mesopore width and specific pore volume when compared to the air-dried material. Hence, during the timescale of 50–123 days, slower drying allows more contraction, resulting in a less porous gel. In order to investigate a potential influence on the drying rate during solvent exchange, Al_2O_3 lyogels were prepared, refluxed in acetone, and dried in a desiccator. Only the amount of drying rate was changed (1, 2, 3 and 4 gmmol^{-1} , based on n_{Air} , respectively). The relative masses of these gel bodies during drying is shown in Figure 3a, the pore width distribution and specific cumulative pore volume of a selection of xerogels in Figure 3b. Averages and standard deviations from Hg porosimetry data of the xerogels are given in Table S1 in the ESI. Indeed, the drying rate can be adjusted by a change of the drying agent mass per mole metal. However, mesopore- and macropore widths as well as specific meso- and macropore volume of all the samples from the measurement series are within the experimental error (Table S1 in ESI). Therefore, during the timescale of < 18 days, the drying rate does not affect the pore system. The inverse effect, *i.e.* an influence of the pore width on the drying rate, is more plausible, though probably less important than the saturation vapor of the pore fluid.

Figure 3b emphasizes the high reproducibility of the synthesis applied here, in particular in terms of the macropore structure. Following the analysis in this section, a change of the Al_2O_3 xerogel monolith mesopore width is possible by solvent exchange and aging. Solvent exchange, however, enables an adjustment of mesopore width from 7.6 nm to 10.5 nm without changing the specific mesopore volume.

Influence of calcination temperature on the pore system

Different from solvent exchange and drying, a change of calcination temperature is a simple, and therefore common method to change the pore structure of mesoporous materials. In fact, such an adjustment has already been reported for Al_2O_3 xerogels with hierarchical meso-/macropore system from polymerization-induced phase separation.^[14,16] In both of the cited sources, only a minor impact of calcination temperature on the macropores was reported. However, a decrease of specific mesopore volume, increase of mesopore width and therefore decrease of specific surface area with increasing calcination temperature was observed. In both cases, this loss of pore volume has been explained by sintering of the Al_2O_3 nanoparticles forming the skeleton of the gel. This is plausible since it was accompanied by a significant broadening of the mesopore width distribution.

The dependence of the pore system on the calcination temperature was also studied for Al_2O_3 xerogels in this article. To avoid experimental variability between different monoliths, a large, 64 mmol Al_2O_3 lyogel was prepared, exchanged with EtOH in solvent bath and dried in a desiccator. The material heat-treated at different temperatures was then investigated by N_2 sorption and Hg porosimetry. N_2 sorption isotherms and corresponding pore width distributions from these studies are shown in Figure 7. The pore width distribution and specific cumulative pore volume determined by Hg porosimetry are given in Figure S2 in the ESI. Quantitative data from analysis of textural properties is given in Table 3. The dried Al_2O_3 sample contains only a low amount of small mesopores ($<0.2 \text{ cm}^3 \text{ g}^{-1}$, Figure 7a).

Upon calcination, mesopores are formed. An increase of calcination temperature then leads to an increase of the mesopore width, while the specific surface area and mesopore volume decrease (Table 3). At the same time, a mild decrease of macropore width is observed along with a decrease of specific macropore volume. Beyond 973 K, however, the macropores remain unaffected. These findings are consistent with previous studies.^[14,16] Sintering and densification are therefore also observed for the Al_2O_3 xerogels in this study.

The mesopore width can therefore also be adjusted by a change of the calcination procedure. However, this will also change the specific pore volume, different from solvent exchange. Nevertheless, by a combination of appropriate solvent exchange and calcination protocols, it should be possible to highly control both mesopore width and specific mesopore volume of Al_2O_3 xerogels.

Application of Ni/ Al_2O_3 xerogel in CO_2 methanation with H_2

To evaluate the potential of the prepared Al_2O_3 xerogels for catalytic applications, the material, which underwent solvent exchange by reflux in acetone and was dried in desiccator over molecular sieves (see Figure 2), was chosen. Powder of this material calcined at 973 K, referred to as " Al_2O_3 support", was loaded with 8.3 wt.% Ni by incipient wetness impregnation

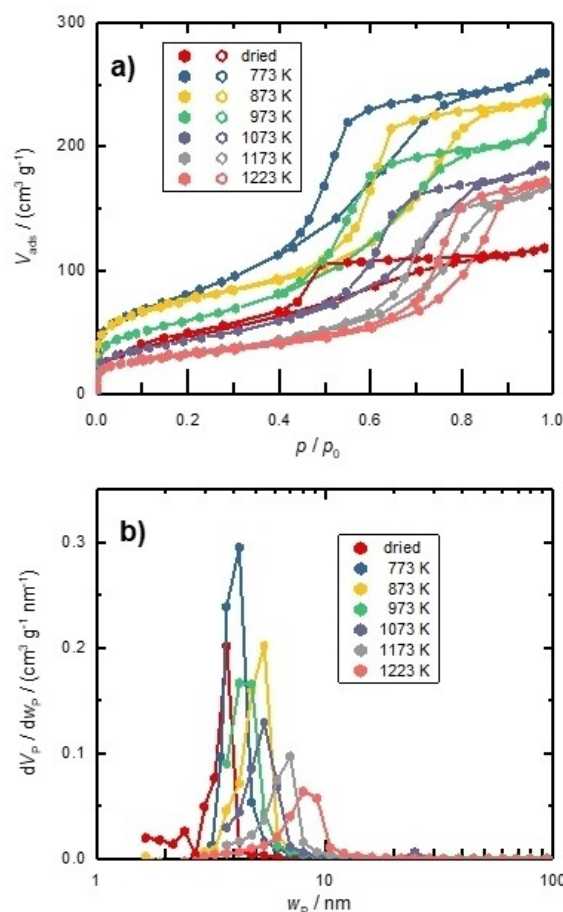


Figure 7. Al_2O_3 xerogels calcined at different temperatures; a) N_2 sorption isotherms, adsorption branch represented by closed, desorption branch represented by open symbols; b) pore width distribution, determined by N_2 sorption.

Table 3. Mesopore width ($w_{p,\text{meso}}$), macropore width ($w_{p,\text{macro}}$), specific mesopore volume ($V_{p,\text{meso}}$) and specific macropore volume ($V_{p,\text{macro}}$) of Al_2O_3 xerogels calcined at different temperatures. Determined by Hg porosimetry.

	$A_{\text{BET}}^{[a]}$ [$\text{m}^2 \text{ g}^{-1}$]	$w_{p,\text{meso}}^{[a]}$ [nm]	$V_{p,\text{meso}}^{[a]}$ [$\text{cm}^3 \text{ g}^{-1}$]	$<w_{p,\text{macro}}^{[b]}$ [μm]	$V_{p,\text{macro}}^{[b]}$ [$\text{cm}^3 \text{ g}^{-1}$]
Dried gel	171	3.7	0.18	1.2	0.67
Calc. 773 K	296	3.9	0.40	1.1	0.70
Calc. 873 K	263	5.4	0.37	1.0	0.61
Calc. 973 K	213	4.7	0.36	1.1	0.52
Calc. 1073 K	156	5.4	0.29	1.0	0.52
Calc. 1173 K	117	7.0	0.26	1.0	0.53
Calc. 1223 K	111	8.1	0.27	1.0	0.50

[a] Determined from N_2 sorption. [b] Determined from Hg porosimetry.

(Figure 8a, referred to as " $8\text{Ni}/\text{Al}_2\text{O}_3$ ") to be compared with an industrial methanation reference catalyst (SPP2080-IMRC, $\omega_{\text{Ni}} = 8.6 \text{ wt.}\%$, Figure 8b),^[35] obtained by an industry partner.

N_2 sorption analysis (Table 4) reveals very similar pore width distributions between the Al_2O_3 xerogel support and SPP2080-IMRC, with $8\text{Ni}/\text{Al}_2\text{O}_3$ showing only a slightly increased pore width (Figure S3 in ESI). However, the xerogel materials exhibit

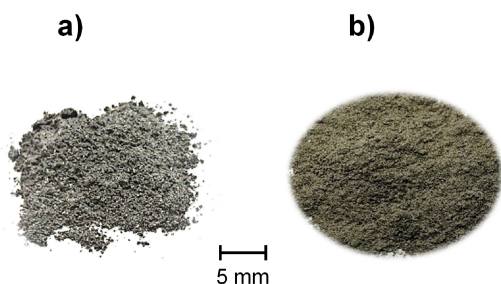


Figure 8. Photographs of a) 8Ni/Al₂O₃ xerogel powder and b) powder of the industrial reference catalyst SPP2080-IMRC.

Table 4. Specific surface area (A_{BET}), specific pore volume (V_p) and pore width (w_p) of the Al₂O₃ support, the Ni-impregnated and calcined 8Ni/Al₂O₃ and the reference catalyst SPP2080-IMRC. Determined by N₂ sorption.

	A_{BET} [m ² g ⁻¹]	V_p [cm ³ g ⁻¹]	w_p [nm]
Al ₂ O ₃ support	284	0.70	9.2
8Ni/Al ₂ O ₃	214	0.59	10.6
SPP2080-IMRC	144	0.40	9.2

both higher specific surface area and pore volume compared to SPP2080-IMRC.

Despite a very similar Ni loading, the H₂-TPR profiles of the catalysts are different (Figure 9). SPP2080-IMRC shows two notable peaks, of which one (523 K) is close to the reduction temperature of a physical mixture of NiO and Al₂O₃ (545 K), indicating some bulk NiO. Additionally, a larger, broad peak at a higher reduction temperature (791 K) is present. This likely arises from the reduction of the small (< 2 nm) NiO nanoparticles found on the material,^[35] which interact more strongly with the support than bulk NiO.

The presence of NiO particles in 8Ni/Al₂O₃ was investigated by Powder X-Ray Diffraction (XRD) and Transmission Electron Microscopy (TEM). An X-ray powder diffractogram (Figure S4 in ESI) did not reveal any NiO reflections, because of the porous nature of the material and relatively low crystallinity

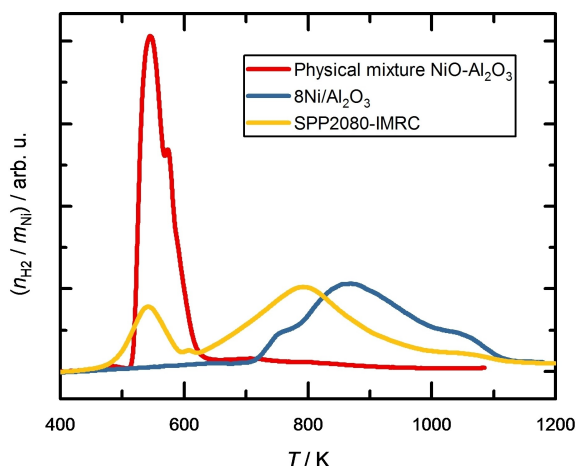


Figure 9. TPR profiles of a physical mixture of NiO with the Al₂O₃ support ($\omega_{\text{Ni}} = 8.2$ wt-%), 8Ni/Al₂O₃ and SPP2080-IMRC.

of the Al₂O₃ support resulted in low intensities. Neither was it possible to distinguish NiO particles from the support material through diffraction or material contrast by TEM (Figure S5 in ESI). However, Energy Dispersive X-ray spectroscopy (EDX) analysis confirmed Ni loadings identical to ICP-OES-data (Tab. S2 in ESI). Therefore, NiO particles may be very small and essentially atomically dispersed across the Al₂O₃ surface. Alternatively, Ni atoms may have been incorporated into the Al₂O₃ framework, similar to earlier findings,^[13] which were derived from a co-gelled Ni/Al₂O₃ catalyst. Considering the substantially lower calcination temperature and time of 773 K and 2 h compared to 1123 K and 8 h used in that study,^[13] Ni penetration into the Al₂O₃ framework is less likely at the conditions applied here. Therefore, 8Ni/Al₂O₃ is assumed to contain very small NiO particles finely dispersed across the material surface.

This explanation is supported by the H₂-TPR curve obtained for 8Ni/Al₂O₃ (Figure 9). In difference to SPP2080-IMRC, it exhibits only one broad reduction peak with a maximum at 870 K and shoulders at both lower and higher temperatures, confirming the absence of bulk NiO on this material. The peak shape of 8Ni/Al₂O₃ appears to resemble the second peak of SPP2080-IMRC but is shifted towards higher reduction temperature. This result is consistent with the assumption, that 8Ni/Al₂O₃ contains a distribution of NiO particles, which on average are even smaller compared to SPP2080-IMRC, thus interacting more strongly with the Al₂O₃ support. Integration of the TPR curves revealed H₂ consumptions of 13.3 mmol g⁻¹ and 15.2 mmol g⁻¹, based on m_{Ni} , for 8Ni/Al₂O₃ and SPP2080-IMRC, respectively. Hence, in addition to the higher reduction temperature of 8Ni/Al₂O₃, a lower fraction of the Ni atoms present in the material is reduced by the TPR experiment. Thus, it can be concluded that SPP2080-IMRC exhibits superior reducibility than 8Ni/Al₂O₃.

Figure 10 shows the temperature-dependence of CO₂ conversion and CH₄ selectivity of the Ni-containing materials during the catalytic experiments. Therein, the temperature between 573 K and 723 K represents a region, in which both catalysts are active, and which is sufficiently far away from the thermodynamic equilibrium. Although qualitatively similar trends are observed, both CO₂ conversion (Figure 10a) and CH₄ selectivity (Figure 10b) of SPP2080-IMRC are higher compared to 8Ni/Al₂O₃ within this region, indicating an overall slightly higher catalytic activity. This difference in activity can be explained by the higher Ni loading and enhanced reducibility of SPP2080-IMRC compared to 8Ni/Al₂O₃. It is reasonable to assume that an optimized Ni loading procedure for the Al₂O₃ support can yield a catalyst with NiO particles activated at lower temperatures, which in turn is expected to improve the catalytic activity. However, this is beyond the scope of this article and should be a subject of further studies.

It should be noted, however, that the relatively small catalyst particle size of 100–300 μm used in this study (generated from the monolith) does not allow valid statements on potential mass transfer limitations in the experiments. Nevertheless, for the SPP2080-IMRC catalyst, catalytic studies have already demonstrated, that substantial mass transfer

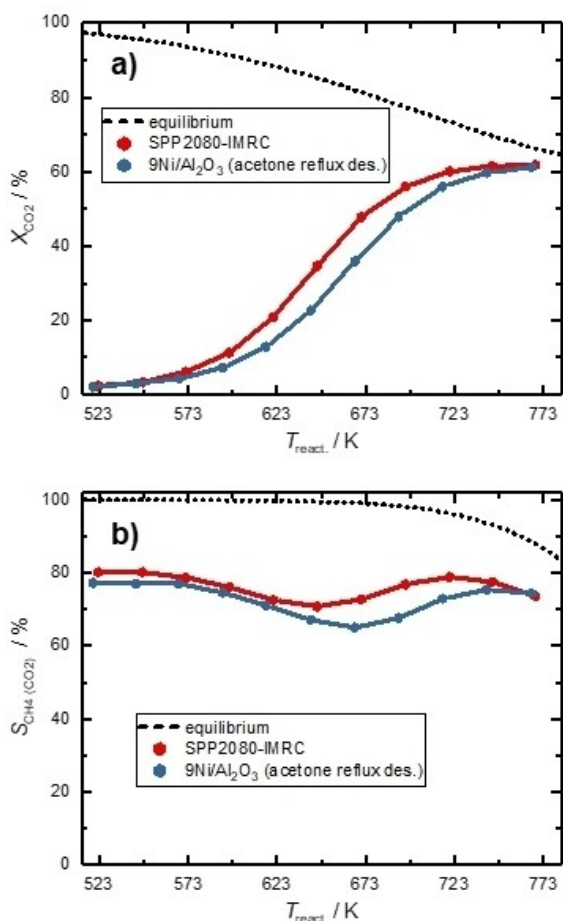


Figure 10. a) CO₂ conversion and b) CH₄ selectivity as a function of reaction temperature in the catalytic CO₂ methanation with H₂ over 8Ni/Al₂O₃ and SPP2080-IMRC.

limitations, which halved the CO₂ conversion at 773 K, occurred, if the original, 2.5 mm-sized catalyst pellets are used instead of a milled powder.^[35] This limitation is a result of the pore system of SPP2080-IMRC. Although it can be considered as hierarchical, the macropores inside the pellets are largely isolated, and only interconnected through mesoporous channels.^[35] Thus, the main transport resistance is located inside the mesopores, where Knudsen diffusion prevails at the given conditions. On the contrary, SEM micrographs of the Al₂O₃ support and 8Ni/Al₂O₃ (Figure 6) clearly demonstrate the hierarchical pore network of the Al₂O₃ xerogels. In these, macropores form a three-dimensional network through the materials. The mesopores are located inside the pore walls and thus connected by the macropores. For this reason, the main transport resistance is within the macropores, in which molecular diffusion prevails. Hence, as molecular diffusion is faster than Knudsen diffusion, a more efficient mass transport is realized in xerogels, in comparison to SPP2080-IMRC.

In earlier work, we calculated the effectiveness factors for spherical catalyst pellets ($d=2.5$ mm) of a purely mesoporous Ni/Al₂O₃ xerogel catalyst and a hierarchically meso-/macroporous Ni/Al₂O₃ xerogel catalyst by solving the mass balance

equations.^[13] The calculations were based on experimental porosity data on Ni-containing Al₂O₃ xerogels prepared through the same sol-gel approach as in this study, though co-gelation was used to introduce Ni. Our results clearly indicated that mass transfer limitations restrict the activity of a purely mesoporous catalyst, while the introduction of macropores leads to a substantial increase of the effectiveness factor. Therefore, the hierarchical mesopore system of 8Ni/Al₂O₃ is well suited to sustain high CO₂ methanation activity, even if mm-sized pellets are used.

Conclusions

Avoiding drying stress is essential for the preparation of mechanically stable, cm-sized Al₂O₃ xerogel monoliths with hierarchical meso-/macropore system. This can be achieved by a combination of solvent exchange and controlled drying. Refluxing is an effective solvent exchange method, while placing the lyogels in a desiccator over molecular sieve leads to fast, yet gentle and reproducible drying. Consequently, cylindrical, cm-sized Al₂O₃ lyogels refluxed in acetone can be dried within a desiccator in just 5 days, overcoming shrinkage of 76 vol.% during drying alone.

Besides its impact on drying, solvent exchange allows an adjustment of the mesopore width, while the macropores of the hierarchical pore system remain unchanged. This is driven primarily by the different surface tension of the solvents within the mesopores, though compression due to syneresis may contribute, if gel bodies are heated up beyond the aging temperature during solvent exchange. Thus, by simply changing the pore fluid at the lyogel stage of a sol-gel-synthesis, an adjustment of the mesopore width from 7.6 nm to 10.5 nm was achieved. Similarly, the mesopore width can be changed by a variation of calcination temperature, although this also affects the specific mesopore volume, owing to sintering of Al₂O₃ nanoparticles.

The degree of control over the mesopore system offered by varying only the post-gelation synthesis parameters emphasizes their vital importance for the design of textural properties of porous materials. The fact that the present findings are well consistent with the current understanding of sol-gel synthesis, as mainly developed for SiO₂-type materials, demonstrates the applicability of the current models for gel drying also to Al₂O₃. These results may be extended also to other types of porous materials, highlighting that defined post-gelation procedures deserve more attention for materials prepared from sol-gel-synthesis in future.

Catalytic studies of a Ni-impregnated Al₂O₃ xerogel demonstrate the applicability of the Al₂O₃ monoliths as a catalyst support. Furthermore, considering the possibility to prepare the Al₂O₃ xerogel monoliths with a controllable hierarchical pore system even up to the cm size range, we consider this material as a well-suited catalyst support, e.g., for CO₂ methanation catalysts based on Ni. Future studies should be extended to a non-uniform active phase and permeability (or diffusivity)

distribution and apply the hierarchical monolithic catalysts under dynamic catalytic conditions.

Experimental Section

Al₂O₃ xerogel preparation

Chemicals used were aluminum chloride hexahydrate (AlCl₃·6H₂O, 99%, AlfaAesar), polyethylene glycol MW 900,000 (PEG-900k, AlfaAesar), (±)-propylene oxide (PO, 99.5%, Acros Organics), ethanol (EtOH, for gelation: absolute, VWR; for solvent exchange: 99.5% denaturated with 1% butan-2-one, VWR); acetone (99.5%, OQEMA) *n*-pentane (99%, VWR), Ni(NO₃)₂·6H₂O (98%, Aldrich), NiO nanopowder (99.8%, Aldrich) and SiC (46 grit, abcr GmbH).

The Al₂O₃ xerogel synthesis was adapted from Herwig et al.^[27] and scaled to a 32 mmol Al₂O₃ default synthesis. A polymer stock solution was prepared by dissolving 6.613 g PEO in 326.40 g EtOH and 285.99 g H₂O. For each gel, 7.725 g AlCl₃·6H₂O were dissolved in an aliquot of 15.098 g of this stock solution in a polypropylene container ($V=60\text{ cm}^3$, $d=33\text{ mm}$), resulting in molar ratios of $n_{\text{Al}}/n_{\text{PEO}}/n_{\text{EtOH}}/n_{\text{H}_2\text{O}}=1/5.6\cdot 10^{-6}/5.4/18.1$. The solution was cooled in an ice bath to 274 to 276 K. Then, 11.52 g of propylene oxide (PO), representing a molar ratio of $n_{\text{Al}}/n_{\text{PO}}=3.1$, were added rapidly under vigorous stirring (800 rpm). The solution was stirred for 3 min in the ice bath, followed by 7 min of stirring at room temperature. The container was then sealed and kept in a H₂O bath at 313 K until gelation. Afterwards, the gel was aged at 328 K for 24 h.

32 mmol Al₂O₃ xerogels presented in this article differ only by the post-gelation treatments solvent exchange following aging. Lyogels underwent either no solvent exchange or were exchanged with EtOH, acetone or *n*-pentane. Solvent exchange with 10.4 mL solvent per mmol Al was conducted either by keeping the gels in a closed solvent bath at room temperature for 7 days, referred to as "bath", or by refluxing them in a sulfonation flask for 24 h, referred to as "reflux". Drying was conducted either under ambient air in closed polypropylene containers ($V=125\text{ cm}^3$, $d=70\text{ mm}$) with 25 holes ($d=0.9\text{ mm}$) punctured through the lid, referred to as "air". Alternatively, lyogels were dried in a desiccator ($V\sim 100\text{ cm}^3$ per mmol Al) over 13X molecular sieves (pellets, $d=1\text{--}2\text{ mm}$, Thermo Scientific), referred to as "des.". The default mass of drying agent was 4 g mmol⁻¹ based on n_{Al} and varied to 1, 2 and 3 g mmol⁻¹ for studies on the drying rate. The drying agent was changed every 7 days. Drying proceeded until weight constancy. After drying, Al₂O₃ gels were calcined in ambient air at 973 K for 8 h using a heating rate of 2 K min⁻¹.

During drying, the mass, diameter, and height of the cylindrical 32 mmol Al₂O₃ monoliths were recorded at least every 3–4 days. The monolith volume was calculated assuming strict cylindrical geometry of the gel bodies. The relative masses and gel bodies were calculated based on the initial monolith mass and volume. In order to determine an experimental error for mass, volume, pore widths and specific pore volumes, each combination of solvent, solvent exchange method and drying method was applied three times to prepare 3 replicates. For data evaluation, the average and standard deviation of relative mass, relative volume, mesopore width, macropore width, specific mesopore volume and specific macropore volume over the three replicates was calculated for each post-gelation treatment combination.

For the investigation of the impact of the calcination temperature on the textural properties, a larger, 64 mmol Al₂O₃ monolith was prepared according to the method described above (polypropylene container with $V=125\text{ cm}^3$ and $d=52\text{ mm}$). The monolith under-

went solvent exchange with EtOH at room temperature for 7 days and was dried in a desiccator over molecular sieves. After drying, the solid was separated into 7 parts. One part was dried at 383 K for 12 h using a heating rate of 2 K min⁻¹. The other parts were calcined at 773 K, 873 K, 973 K, 1073 K, 1173 K and 1223 K for 8 h using the same heating rate.

Preparation of Ni-containing Al₂O₃

A sample of an Al₂O₃ xerogel monolith refluxed in acetone and dried within a desiccator was ground and sieved to a fraction of 100–300 μm particle size (referred to as "Al₂O₃ support"). The Al₂O₃ support was impregnated with an aqueous solution of Ni(NO₃)₂·6H₂O ($c=1.33\text{ mol L}^{-3}$) by the incipient wetness method with a target load of 9 wt.%, assuming an absorption capacity of 1300 cm³ liquid per g support. Following impregnation, the solid was dried at 383 K for 12 h and calcined at 773 K for 2 h, both using a heating rate of 2 K min⁻¹. The catalyst prepared in this way is referred to as "8Ni/Al₂O₃", indicating the experimentally measured Ni mass fraction. For comparison, a physical mixture of NiO and Al₂O₃ with a target Ni mass fraction of 9 wt.% was prepared by grinding an appropriate mass of NiO nanopowder and the Al₂O₃ support to a homogenous solid.

An industrial methanation reference catalyst (SPP2080-IMRC) comprised of Ni-loaded Al₂O₃ pellets ($d=2.5\text{ mm}$), was obtained from a chemical company. Prior to use, these pellets were ground in a Retsch PM 100 planetary ball mill with ZrO₂ balls at 450 rpm for 5 min and sieved to a fraction of 100–300 μm.

CHN elemental analysis

CHN elemental analysis was conducted on a Vario EL MICRO element analyzer manufactured by Heraeus. Samples were crimped within a container made of aluminum and analyzed via heat extraction.

Hg porosimetry

Hg porosimetry analysis was conducted on a Pascal 140 (ThermoScientific) for data points from pressures up to 250 kPa and a Pascal 440 (ThermoScientific) for data points from pressures between 250 kPa to 400 MPa. The contact angle used was 140° with a surface tension of 0.48 N m⁻¹. The pore width was calculated by the Washburn equation from the intrusion curve.^[36] The meso- ($w_{\text{P,meso}}$) and macropore width ($w_{\text{P,macro}}$) correspond to the modal mesopore width and modal macropore width, respectively. An experimental error of 5% is expected for specific pore volumes and pore widths. Prior to analysis, samples were ground and sieved to a fraction of 100–300 μm diameter particle size.

Nitrogen sorption

N₂ sorption experiments were conducted on a BELSORP-miniX instrument. Samples were degassed at 523 K for at least 6 h. The adsorption and desorption isotherms were recorded at 77 K and analyzed using the BELSORP BELMaster™ software (total pore volume determined at $p/p_0 \geq 0.99$). Specific surface area and pore width distribution were determined by the BET method^[37] ($p/p_0=0.05\text{--}0.30$, adsorption branch) and BJH method^[38] (desorption branch), respectively. An experimental error of 5% is expected for specific surface area, specific pore volume, and pore width.

Inductively coupled plasma optical emission spectrometry (ICP-OES) ICP-OES was conducted using an Optima 8000 instrument

(Perkin Elmer) equipped with a Scott/crossflow sample injection system. Samples were dissolved in a mixture of hydrofluoric (47–51 wt.%, Normatom, VWR), nitric (67–90 wt.%, Normatom, VWR), and hydrochloric acid (34–37 wt.%, Normatom, VWR) in an Multi-wave 3000 (Anton Paar) microwave prior to analysis.

Temperature-programmed reduction with H₂ (H₂-TPR)

H₂-TPR analysis was performed on a BELCAT II catalyst analyzer (MicrotracBEL Corp.) equipped with a thermal conductivity detector (TCD) and a H₂O trap. For a typical experiment, 50 mg catalyst was placed inside the quartz glass reactor. The sample was activated at 573 K for 15 min in an O₂-Ar mixture ($F_{O_2}/F_{Ar}=1/4$) of a total flow rate of 30 cm³ min⁻¹. Then, the flow was switched to pure Ar with a total flow rate of 20 cm³ min⁻¹, and the instrument was allowed to equilibrate for 20 min. Finally, using a H₂-Ar mixture ($F_{H_2}/F_{Ar}=1/9$) and a total flow rate of 30 cm³ min⁻¹, the reactor was heated to 1173 or 1223 K at a heating rate of 10 K min⁻¹ and kept at the final temperature for 20 min.

Electron Microscopy

Scanning electron microscope (SEM) was carried out using a LEO Gemini 1530 (Zeiss) operated at an acceleration voltage of 10 kV. Transmission electron microscopy (TEM) analysis was performed at a JEM-2100Plus instrument (Jeol) operated at an accelerating voltage of 200 kV. The TEM was equipped with a LaB₆ cathode and high-resolution pole piece to achieve a point resolution in TEM mode of 0.23 nm. The images were recorded with a 4 K CMOS camera (TVIPS) and EDX analysis was done by Octane T Optima (EDAX) windowless silicon drift detector. Sample preparation for TEM was performed by grinding in EtOH (99.5% denaturated with 1% butan-2-one, VWR) and the dispersed particles were supported on a holey carbon Cu-TEM grid.

X-Ray Powder Diffraction (XRD)

Powder XRD patterns were recorded using a Huber G670 Guinier geometry diffractometer equipped with an image-plate detector. Reflections were recorded between $2\theta=4^\circ$ and $2\theta=100^\circ$ using Cu-K α radiation ($\lambda=0.15406$ nm), with a step size of 0.005° and an irradiation time of 30 min per scan.

Catalytic experiments

The catalytic activity was determined in fixed-bed reactor with 25 mg catalyst powder (100–300 μ m) diluted ($m_{cat}/m_{SiC}=1/9$) in silicon carbide powder (46 grit, abcr GmbH) in a quartz glass tube with an inner diameter of 8 mm, an outer diameter of 10 mm, and a length of 40 cm. The powder mixture was fixed with quartz glass wool from both sides. Additionally, 0.5 g silicon carbide was placed in front of the powder mixture to ensure isothermal and uniformly distributed gas flow. The silicon carbide was also kept in place by quartz glass wool. Type K thermocouples were placed before and behind the packing. The latter was considered as reaction temperature. After the glass tube was placed into a furnace and sealed, gases (CO₂ purity 3.0, H₂ 5.0, He 5.0, Westfalen AG) were supplied via mass flow controllers (El-Flow® Select, Bronkhorst Deutschland Nord GmbH). The product gas was cooled down to 276 K to condensate H₂O and a constant flow of 15 Ncm³ min⁻¹ N₂ (purity 5.0, Westfalen AG) was added as internal standard. Potentially remaining H₂O was separated with a membrane before the product gases. The gas flow rates of CO₂, CO and CH₄ were determined by

gas chromatography (490 Micro GC System, Agilent Technologies, Inc.).

Before the catalytic activity measurements were conducted, the catalysts were dried at a furnace temperature of 393 K with 120 Ncm³ min⁻¹ of a mixture of H₂ and He ($F_{H_2}/F_{He}=1/1$). Afterwards, the furnace temperature was increased to 673 K and the catalyst was reduced for 8 h under the same gas composition. Subsequently, the catalyst was aged at reaction conditions ($F_{CO_2}=20$ cm³ min⁻¹, $F_{H_2}=80$ cm³ min⁻¹, $F_{He}=100$ cm³ min⁻¹, $p=1.2$ bar) at 773 K for 8 h. Five product gas samples were taken at each furnace temperature, following a step change profile from 773 K to 523 K in steps of 25 K. The temperature difference before and behind the packing was below 7 K and the furnace temperature was up to 15 K higher than the reaction temperature. The carbon balance was closed to more than 99% in all cases.

Acknowledgements

Financial support for this work by Deutsche Forschungsgemeinschaft (DFG, German Research Foundation) via the priority program SPP2080 (projects no. GL 290/13-1, SU 189/8-1) is gratefully acknowledged. K.L.A. also acknowledges support from the Leipzig Graduate School of Natural Sciences "Building with Molecules and Nano-objects (BuildMoNa)". Thanks are also due to Leoni Lieder for assistance in the synthetic work. Likewise, Manuela Roßberg, Heike Rudzik, Sebastian Geisler, Eike Sebastian Welter, Tim Jähnichen and Stephan Feser are acknowledged for their assistance with CHN, ICP-OES, XRD, H₂-TPR and Hg porosimetry analyses, respectively. Open Access funding enabled and organized by Projekt DEAL.

Conflict of Interest

The authors declare no conflict of interest.

Data Availability Statement

The data that support the findings of this study are available from the corresponding author upon reasonable request.

Keywords: Aluminum Oxide · CO₂ Methanation · Drying · Monoliths · Sol-Gel Synthesis · Solvent Exchange

- [1] V. Masson-Delmotte, P. Zhai, A. Pirani, S. L. Connors, C. Péan, S. Berger, N. Caud, Y. Chen, L. Goldfarb, M. I. Gomis et al., *IPCC, 2021: Summary for Policymakers. In: Climate Change 2021: The Physical Science Basis.*, Cambridge University Press, Cambridge, 2021.
- [2] a) K. Sühsen, M. Hisschemöller, *Energy Policy* 2014, 69, 316; b) P. A. Østergaard, N. Duic, Y. Noorollahi, S. A. Kalogirou, *Renewable Energy* 2021, 179, 877.
- [3] a) K. F. Kalz, R. Kraehnert, M. Dvoyashkin, R. Dittmeyer, R. Gläser, U. Krewer, K. Reuter, J.-D. Grunwaldt, *ChemCatChem* 2017, 9, 17; b) J. Riese, M. Grünewald, *Chem. Ing. Tech.* 2020, 92, 1887.
- [4] C. Miguel, A. Mendes, L. Madeira, *Energies* 2018, 11, 3259.
- [5] S. Rönisch, J. Schneider, S. Matthischke, M. Schlüter, M. Götz, J. Lefebvre, P. Prabhakaran, S. Bajohr, *Fuel* 2016, 166, 276.

- [6] a) D. Schlereth, O. Hinrichsen, *Chem. Eng. Res. Des.* **2014**, *92*, 702; b) D. Türks, H. Mena, U. Armbruster, A. Martin, *Catalysts* **2017**, *7*, 152.
- [7] J. Bremer, K. H. G. Rätze, K. Sundmacher, *AIChE J.* **2017**, *63*, 23.
- [8] J. Bremer, K. Sundmacher, *React. Chem. Eng.* **2019**, *4*, 1019.
- [9] R. T. Zimmermann, J. Bremer, K. Sundmacher, *Chem. Eng. J.* **2020**, *387*, 123704.
- [10] R. T. Zimmermann, J. Bremer, K. Sundmacher, *Chem. Eng. J.* **2022**, *428*, 130771.
- [11] J. Gao, Q. Liu, F. Gu, B. Liu, Z. Zhong, F. Su, *RSC Adv.* **2015**, *5*, 22759.
- [12] a) S. Rahmani, M. Rezaei, F. Meshkani, *J. Ind. Eng. Chem.* **2014**, *20*, 1346; b) M. Aghayan, D. I. Potemkin, F. Rubio-Marcos, S. I. Uskov, P. V. Snytnikov, I. Hussainova, *ACS Appl. Mater. Interfaces* **2017**, *9*, 43553; c) S. V. Moghaddam, M. Rezaei, F. Meshkani, R. Daroughegi, *Int. J. Hydrogen Energy* **2018**, *43*, 19038; d) E. H. Cho, W. Kim, C. H. Ko, W. L. Yoon, *Catalysts* **2020**, *10*, 643.
- [13] S. Weber, K. L. Abel, R. T. Zimmermann, X. Huang, J. Bremer, L. K. Rihko-Struckmann, D. Batey, S. Cipiccia, J. Titus, D. Poppitz et al., *Catalysts* **2020**, *10*, 1471.
- [14] Y. Tokudome, K. Fujita, K. Nakanishi, K. Miura, K. Hirao, *Chem. Mater.* **2007**, *19*, 3393.
- [15] K. Nakanishi, *J. Porous Mater.* **1997**, *4*, 67.
- [16] X. Guo, W. Li, K. Nakanishi, K. Kanamori, Y. Zhu, H. Yang, *J. Eur. Ceram. Soc.* **2013**, *33*, 1967.
- [17] W. Yang, F. Ling, H. Zhang, S. Wang, Z. Shen, *Chem. Lett.* **2019**, *48*, 1274.
- [18] B. Gawel, K. Gawel, G. Øye, *Materials* **2010**, *3*, 2815.
- [19] A. Feinle, M. S. Elsaesser, N. Hüsing, *Chem. Soc. Rev.* **2016**, *45*, 3377.
- [20] a) T. K. Sherwood, *Ind. Eng. Chem.* **1929**, *21*, 12; b) T. K. Sherwood, *Ind. Eng. Chem.* **1929**, *21*, 976.
- [21] a) G. W. Scherer, *J. Non-Cryst. Solids* **1988**, *100*, 77; b) G. W. Scherer, *J. Non-Cryst. Solids* **1989**, *109*, 171.
- [22] C. J. Brinker, G. W. Scherer, *Sol-Gel Science. The Physics and Chemistry of Sol-Gel Processing*, Academic Press Inc., San Diego, **1990**.
- [23] G. W. Scherer, *J. Non-Cryst. Solids* **1992**, *147–148*, 363.
- [24] a) G. Musielak, T. Śliwa, *Transp. Porous Media* **2012**, *95*, 465; b) N. Karagiannis, M. Karoglou, A. Bakolas, M. Krokida, A. Moropoulou, *Constr. Build. Mater.* **2017**, *137*, 441; c) M. Heydari, K. Khalili, S. Y. Ahmadi-Brooghani, *Procedia Manuf.* **2018**, *22*, 811; d) N. Kumar, J. H. Arakeri, *Drying Technol.* **2020**, *38*, 1194; e) O. Maalal, M. Prat, D. Lasseux, *Phys. Fluids* **2021**, *33*, 27103.
- [25] K. Kajihara, *J. Asian Ceram. Soc.* **2013**, *1*, 121.
- [26] E. Tsotsas, A. S. Mujumdar (Eds.) *Modern Drying Technology. Understanding and Preventing Structural Changes during Drying of Gels*, Wiley-VCH, Weinheim, **2011**.
- [27] J. Herwig, J. Titus, J. Kullmann, N. Wilde, T. Hahn, R. Gläser, D. Enke, *ACS Omega* **2018**, *3*, 1201.
- [28] T. Yotsuyanagi, T. Ohkubo, T. Ohhashi, K. Ideka, *Chem. Pharm. Bull.* **1987**, *35*, 1555.
- [29] P. Atkins, J. de Paula, *Physical Chemistry*, W. H. Freeman and Company, New York, **2010**.
- [30] W. M. Haynes (Ed.) *CRC Handbook of Chemistry and Physics*, CRC Press, Boca Raton, FL, **2014–2015**.
- [31] a) R. Takahashi, K. Nakanishi, N. Soga, *Faraday Discuss.* **1995**, *101*, 249; b) R. Takahashi, K. Nakanishi, N. Soga, *J. Non-Cryst. Solids* **1995**, *189*, 66.
- [32] S. Saha, *J. Sol-Gel Sci. Technol.* **1997**, *3*, 117.
- [33] X. Lu, G. Hasegawa, K. Kanamori, K. Nakanishi, *J. Sol-Gel Sci. Technol.* **2020**, *95*, 530.
- [34] S. Weber, A. Diaz, M. Holler, A. Schropp, M. Lyubomirskiy, K. L. Abel, M. Kahnt, A. Jeromin, S. Kulkarni, T. F. Keller et al., *Adv. Sci.* **2022**, *9*, 2105432.
- [35] S. Weber, R. T. Zimmermann, J. Bremer, K. L. Abel, D. Poppitz, N. Prinz, J. Ilsemann, S. Wendholt, Q. Yang, R. Pashminehazar et al., *ChemCatChem* **2022**, *14*, e202101878.
- [36] E. W. Washburn, *Phys. Rev.* **1921**, *17*, 273.
- [37] S. Brunauer, P. H. Emmett, E. Teller, *J. Am. Chem. Soc.* **1938**, *60*, 309.
- [38] E. P. Barrett, L. G. Joyner, P. P. Halenda, *J. Am. Chem. Soc.* **1951**, *73*, 373.

Manuscript received: February 27, 2022

Revised manuscript received: May 17, 2022

Accepted manuscript online: May 23, 2022

Version of record online: June 22, 2022